

Hazardous Base Surges of Taal's 2020 Eruption

Alfredo Mahar Francisco Lagmay (✉ aalagmay@up.edu.ph)

National Institute of Geological Sciences, University of the Philippines

Maria Ines Rosana Balangue

National Institute of Geological Sciences, University of the Philippines

Mario Aurelio

National Institute of Geological Sciences, University of the Philippines

Audrei Anne Ybanez

University of the Philippines Diliman

Richard Ybanez

National Institute of Geological Sciences, University of the Philippines

Jolly Joyce Sulapas

National Institute of Geological Sciences, University of the Philippines

Criselda Baldago

National Institute of Geological Sciences, University of the Philippines

Dana Marielle Sarmiento

National Institute of Geological Sciences, University of the Philippines

Hillel Cabria

Agriculture Sustainability Initiatives for Nature, Inc.

Raymond Rodolfo

Ateneo de Manila University

Dwayne Rafael

National Institute of Geological Sciences, University of the Philippines

Jose Rainier Trinidad

National Institute of Geological Sciences, University of the Philippines

Eligio Obille Jr.

University of the Philippines National Institute for Science and Mathematics Education Development

Neon Tomas Rossel II

Agriculture Sustainability Initiatives for Nature, Inc.

Research Article

Keywords: Taal Volcano, UAV and LiDAR, Earth and other planets, dynamic pressures

Posted Date: April 12th, 2021

DOI: <https://doi.org/10.21203/rs.3.rs-385254/v1>

License:  This work is licensed under a Creative Commons Attribution 4.0 International License.

[Read Full License](#)

Version of Record: A version of this preprint was published at Scientific Reports on August 3rd, 2021. See the published version at <https://doi.org/10.1038/s41598-021-94866-2>.

Hazardous Base Surges of Taal's 2020 Eruption

A.M.F. Lagmay^{1,2}, M.I.R. Balangue-Tarriela¹, M. Aurelio¹, R. Ybanez¹, A. Bonus-Ybanez², J. Sulapas^{1,2}, C. Baldago¹, D.M. Sarmiento¹, H. Cabria³, R. Rodolfo^{3,4}, D.R. Rafael¹, J.R. Trinidad¹, E. Obille Jr.⁵ and N. Rosell II³

¹*UP National Institute of Geological Sciences, College of Science, University of the Philippines, Diliman, Quezon City*

²*UP Resilience Institute and NOAA Center, University of the Philippines, Diliman, Quezon City, Metro Manila,*

³*Agriculture Sustainability Initiatives for Nature, Inc.,*

⁴*Department of Environmental Science, Ateneo De Manila University, Loyola heights, Quezon City, Metro Manila,*

⁵*National Institute for Science and Mathematics Education Development, University of the Philippines, Diliman, Quezon City*

After 43 years of repose, Taal Volcano erupted on 12 January 2020 forming hazardous base surges. Using field, remote sensing (i.e. UAV and LiDAR), and numerical methods, we gathered primary data to generate well-constrained empirical information on dune bedform characteristics, impact dynamic pressures and velocities of base surges to advance our knowledge on this hazard to understand and evaluate its consequences and risks. The base surges traveled at 50-60 km/hr near the crater and decelerated before making impact on coastal communities with dynamic pressures of at least 1.7-2.1 kPa. The base surges killed more

than a thousand livestock in the southeast of Taal Volcano Island, and then traveled another 600 meters offshore. This work is a rare document of a complete, fresh and practically undisturbed base surge deposit, important in the study of dune deposits formed by volcanic, and other processes on Earth and other planets.

1 Introduction

After 43 years of repose, Taal Volcano erupted on 12 January 2020 forming a 17-21-km high plume¹⁻³ causing prolonged widespread disruption to the normal daily activities of surrounding populations. Only one death was directly attributed to the explosive eruption, the body of a person retrieved under ~ 1.5 meters of pyroclastic deposits on the west coast of Taal Volcano Island (TVI). Another man who failed to evacuate from the island is still missing⁴. Considering the sudden and explosive nature of Taal Volcano's 2020 eruption that generated Base Surges, the number of recorded fatalities could have easily been higher.

Base Surges are one of the most lethal and destructive hazards of Taal's historical eruptions⁵. The 1911 eruption killed 1,335 people⁶, whereas the 1965 eruption killed 200⁷. Other eruptive events, such as in AD1716, AD1731, AD1749, and AD1754, were also described to produce Base Surges resulting in thousands of deaths⁸. Out of the 34 identified historical eruptions since AD1572, Taal had six distinct eruptions reported to have generated Base Surges. Here, we report the seventh distinct eruption of Taal Volcano that generated Base Surges. Until the time of this writing, there is no verbal account nor published report on the occurrence of Base Surges from Taal Volcano's 2020 eruption.

The 2020 Base Surges were accidentally discovered during an ecological expedition on the barren Taal Volcano Island (TVI) to search for signs of life and how to make the area productive again⁹. These Base Surges were mapped in the field with the aid of satellite and drone technologies. Pre-eruption Light Detection and Ranging (LiDAR) data and post-eruption Drone Digital Terrain Models (DTMs) were used to measure the thickness and estimate the volume of the latest surge deposits of Taal Volcano. The dune field in the southeast sector offer a rare, largely undisturbed, and nearly complete picture of a base surge deposit field, which we describe concisely in this article. Often, these deposits are studied as discontinuous outcrops years after an eruptive event, when erosion, deposition, and vegetation have obliterated or concealed important features that hinder better understanding of flow emplacement and dynamics¹⁰⁻¹².

Taal Volcano's 1965 eruption was well-documented by J.G. Moore^{7,13}, who after observations of similar basal flows in nuclear blasts, coined the word "Base Surge", a term still used in the volcanological literature and by warning agencies until today¹⁴⁻¹⁶. Base surges are the dilute, wet, and turbulent end-member of Pyroclastic Density Currents (PDCs), which are gravity-driven flows generated by the collapse and lateral spreading of hot gas particle-laden mixtures produced during explosive volcanic eruptions^{17,18}. Base surges form when magma and water interact during phreatomagmatic eruptions^{16,19-24}. As one of the 16 Decade Volcanoes²⁵⁻²⁷ identified by the International Association of Volcanology and Chemistry of the Earth's Interior (IAVCEI), this work on the Taal Volcano 2020 Base Surges is of particular importance because of the destructive nature and proximity of the volcano to densely populated areas. The results can also be used to compare dune deposits formed by volcanic, and other processes on Earth and other planets²⁸⁻³⁰.

2 Results

Analysis of time-series imagery and video analysis The 2020 eruption of Taal Volcano generated a vertical volcanic eruption column consisting of a gas thrust (jet phase), a convective, and an umbrella region³¹. The gas thrust region rose to ~ 130 meters above the Main Crater (MC) rim and is the region where ballistic volcanic bombs and laterally moving flows (basal clouds) traveling at $50\text{-}60\text{ ms}^{-1}$ are observed. In the convective region, ingested air continued to expand the plume reducing its density. This caused the discharging mixture of hot gas and pyroclasts to rise and form a gray-colored column of billowing clouds that thickened upward. By around 4:00 pm, a north-drifting umbrella cloud is well-formed (Figure 1), which by 8:00 pm reached $17\text{-}21\text{ km}^{1-3}$ with an E-W diameter of $\sim 100\text{ km}$. The eruption height and umbrella diameter peg the eruption to have mass discharge rates^{31,32} in the order of 10^7 kgm^{-3} with an equivalent Volcanic Explosivity Index (VEI)=4. Intense activity lasted up to about 10 hours and started to wane in the morning of 13 January 2020 at about 2:49 am when lava fountaining was observed³³. Volcanic activity on 13 January 2020 was characterized by Vulcanian (cannon-like) explosions that were directed towards the west (see supplementary video).

Morphology Remotely sensed images show the entire TVI covered by light gray tephra. Close-up views reveal a distinct mottled texture that arises from dune-like forms, typical of base surge deposits^{7,13}. These dunes were delineated manually from the crater rim to the coast of the island on the southeastern and western slopes. They are also present in areas in the north but do not extend up to the coast of TVI (Figure 2). There are no dunes in the southwest slopes because of the high

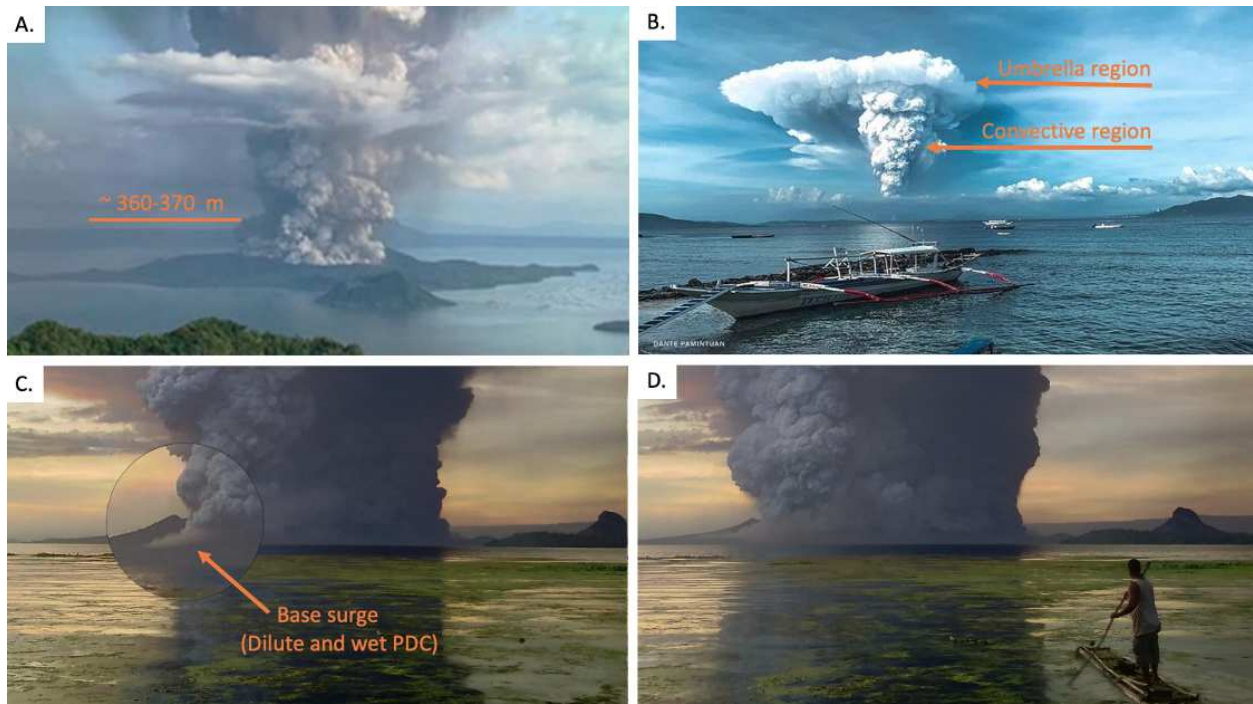


Figure 1: Photographs and screenshots of videos of the 12 January 2020 eruption of Taal. A) Eruption showing a lateral basal cloud with an estimated fountain height of 361 m; B) Umbrella cloud and convective regions; C) Magnified view of Base Surge flows (dilute and “wet” PDCs) forming in the southeast sector of TVI; D) Dust covering the southeastern slopes of TVI. Photo credits: Dante Pamintuan, CNN News and Andres Alisuag.

elevation of the main crater rim in the southwest. The distribution suggests radial spreading of the base surges as a result of column collapse¹³ with possible contribution from discrete “cocktail jets” and “eruption slugs”^{19–21,23}.

The southeast sector is characterized by a desert dune field (Figure 2) and incised channels from water erosion. The larger incised channels or gullies generally follow pre-eruption drainage channels whereas the smaller incised channels are mainly controlled by the dune relief. Larger dunes bear erosion marks that resemble a trellis drainage pattern that connect to smaller incised channels at the base of and in between dunes. These smaller incised channels, in turn, connect to larger gullies.

Base surge dunes in the eastern sector of TVI are generally oriented parallel to the southeast crater rim and are most prominent at the mid-slopes. The ratio of dune wave height (0.12-0.80 m) and wavelength (1.1-9.0 m) scales down towards gentler slopes at low elevations (Figure 3) with wave height decreasing progressively, which reflects waning of the density current. The ratios of wave height to wavelength plot partly within the field of base surges (moist PDCs) in dunes studied worldwide³⁴. This field of moist PDCs in the diagram is hereby expanded because of the morphometry of dunes in the mid-slopes and those near the coast, which exhibit smaller wave height to wavelength ratios.

Dunes are asymmetrical with the stoss side invariably shorter than the lee side (Figure 3). When measured relative to the horizontal plane, the stoss side of dunes have gentler slopes compared to their lee side along steep slopes of the volcano. Nearer to the coast where the volcano

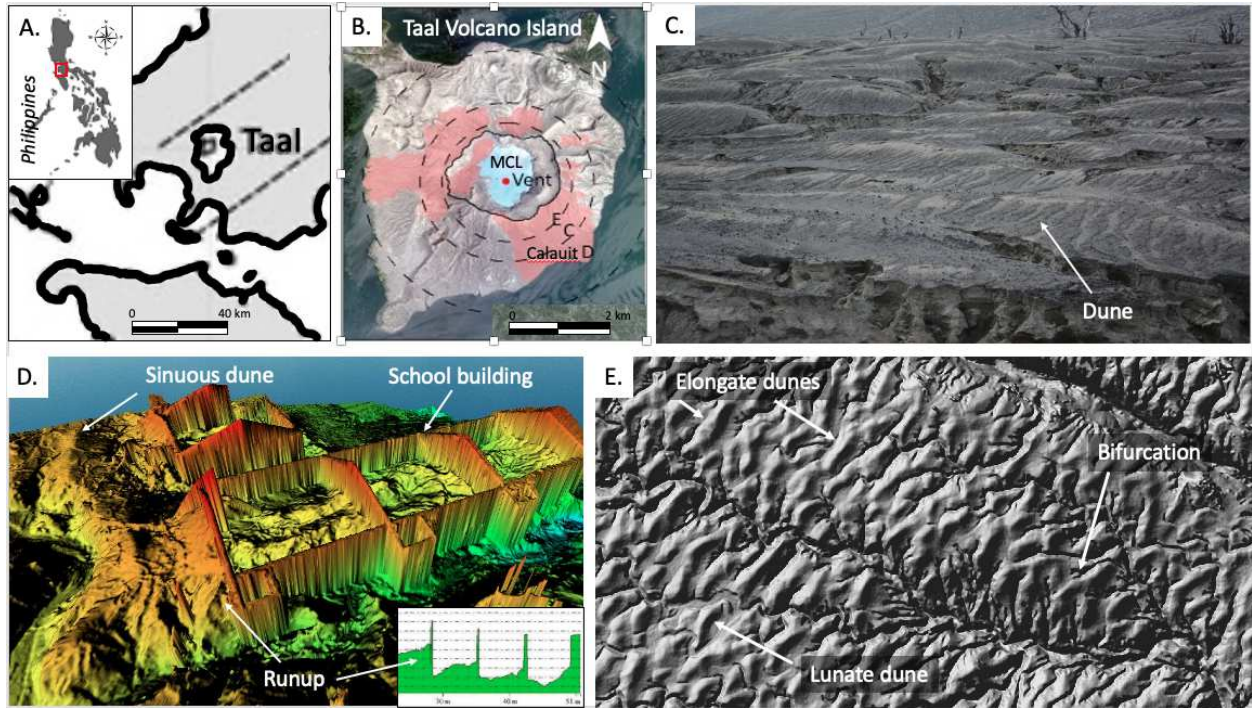


Figure 2: Dunes of TVI. A) General location of Taal Volcano Island. B) Distribution of the 2020 base surge dunes. Circles refer to upper slope, middle slope and lowerslope boundaries. C) Photograph of the dune field. D) Digital Surface Model of school overwhelmed by base surges. Sinuous dunes and runup of the base surge also occur inside the classrooms. E) Plan view image of dunes showing elongate and lunate dunes. Bifurcation of dunes are also shown.

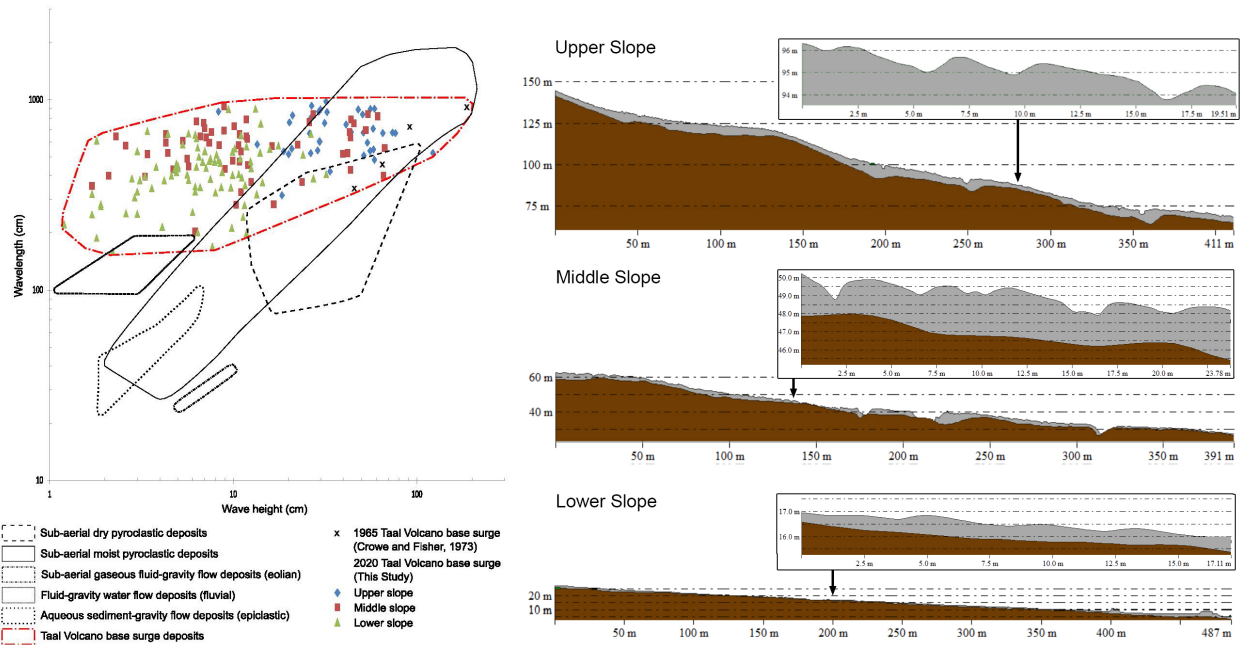


Figure 3: A) Graph of dune waveheight vs wavelength for subaerial dry and moist pyroclastic flows, eolian, fluvial and aqueous sediment-gravity (epiclastic) flows. Modified from Moorehouse and White (2016)³⁴; B) Thickness of surge deposits in the upper, middle and lower slopes of the southeast sector of TVI. Profiles also show dunes with measured angles of stoss and lee sides at different gradients of underlying slope.

gradient is nearly flat, the stoss side is steeper than the lee side. However, when stoss and lee angles are measured relative to the dip angle of the underlying slope, steepness of the stoss is always higher than the lee side of dunes. This observation where the underlying topography affects the measurement angle of the stoss and lee sides has implications to the study of outcrops of old dune formations produced by dilute PDCs. When not recognized, this may lead to difficulties in the interpretation of flow direction and formation mechanisms of bedforms ^{10,12,35}.

Dune bedforms are mostly elongated with lengths ranging from 3.9 - 44.7 m and are sinuous or lunate in planform. Lunate dunes¹⁰ are dominantly crescent-shaped and concave downstream. They are commonly found at the lower slopes whereas sinuous dunes are more abundant at the middle and upper slopes. Occasional bifurcation of dunes were also observed. Dune bedforms are not readily apparent in the area a few tens of meters from the crater rim but closer examination reveals the presence of slight bulges on the surface with underlying cross-bedded structures.

Thickness and volume Based on the analysis of pre- and post-2020 eruption DTMs of the southeast sector of TVI, the base surge deposits of Taal Volcano are thickest on the upper slopes (53-182 m elevation) where the gradient is on average about 17°. The maximum and average thickness on these slopes are 12.3 m and 4.7 m, respectively (Figure 3). In the middle part of the southeast sector (21-76 m elevation), where the average slope gradient is 13°, the maximum thickness is 11.0 m whereas the average thickness is 2.6 m. The lower slopes near the coast (4-26 meters elevation), with an average gradient of 8° have the thinnest deposits with a maximum and average thickness of 10.5 m and 1.0 m, respectively.

The base surge deposits drape differentially over undulating topography. Deposits are relatively thin at the crest of hills becoming thicker at its base. This is observed almost everywhere in the dune field except for an area where there is a conspicuous topographic bulge at the lower half of the upper-slope section (Figure 3). Upon closer examination in topographic profiles, this sudden change in relief reflects the frontal edge of an older pre-2020 PDC deposit draped by new deposits. In this area, dilute PDC deposits are thick at the top of the old deposit and abruptly become thin downslope of the bulge. Sudden thinning of the deposit downstream of the bulge may be due to the pre-existing gully that channelled the base surge or due to air entrainment as the current jumped over the bulge favoring suspension. In other areas of the lower slopes, base surge deposits become thinner immediately upon crossing a pre-eruption river channel (Figure 3). The deposit thickens after a few tens of meters and suddenly thin out again after another river channel is crossed.

The estimated minimum volume of the base surge deposits on TVI, which cover an area of 6.2 million m² (Figure 2), is 16-21.5 million m³ with a Dense Rock Equivalent (DRE)³⁶ of 8.4-11.3 million cubic meters. The thickness of the deposit at the coast is 2.0 m, which indicates that the base surges reached the outer lake. Based on the extent of base surge dunes in the west, our calculations placed the end of the density current in the southeast sector ~600 m offshore the village of Calauit.

Stratigraphy and componentry The stratigraphy of the 2020 Base Surge deposits in southeast TVI is composed of alternating undulating beds and laminae which are, in general, relatively coarser near the crater compared to those near the coast (Figure 5). This suggests that the den-

sity currents were losing energy and carrying capacity as they traveled downslope. When foresets and backsets of beds and laminae of non-uniform thickness connect, they form dunes. Laterally continuous, horizontal planar beds with equal thickness and well-sorted components are less pervasive. When present, they indicate the contribution from fall out of pyroclasts. The presence of accretionary lapili in almost all of the deposits, plastered deposits on vertical walls, as well as abundance of juveniles and accidental clasts, constitute strong evidence that suggests a wet density current formed from water-magma interaction¹⁶.

The pre-2020 eruption topography is marked by the presence of plant debris. Overlying the unconformity is a poorly sorted 0.2-m bedded tephra deposit dominated by ash-sized pyroclasts. This bed is overlain by cross-bedded deposits dominated by lapilli-sized rock and crystal fragments. Some of the tephra layers show grading, both normal and reverse. The number of irregularly stacked dunes is variable, ranging from 1-4 dune bed forms of variable sizes with outcrops in the mid-slope having the most number in a stack. In between stacked dunes are differential draping beds that fill the trough between laterally adjacent dunes. Laminae composed of poorly-sorted finer-grained tephra cap the dunes. Overall, there is an increase in the proportion of fine components in strata towards the top of each outcrop. These stratified beds and laminae of the surge deposits are believed by many to have formed from numerous explosions that generate particle-laden density currents that vary in velocity during transport^{35,37-40}. Lastly, the size-frequency distribution in all sampled beds indicate poor sorting reflective of deposition from a density current. Some beds exhibit a weakly bimodal distribution (Figure 4).

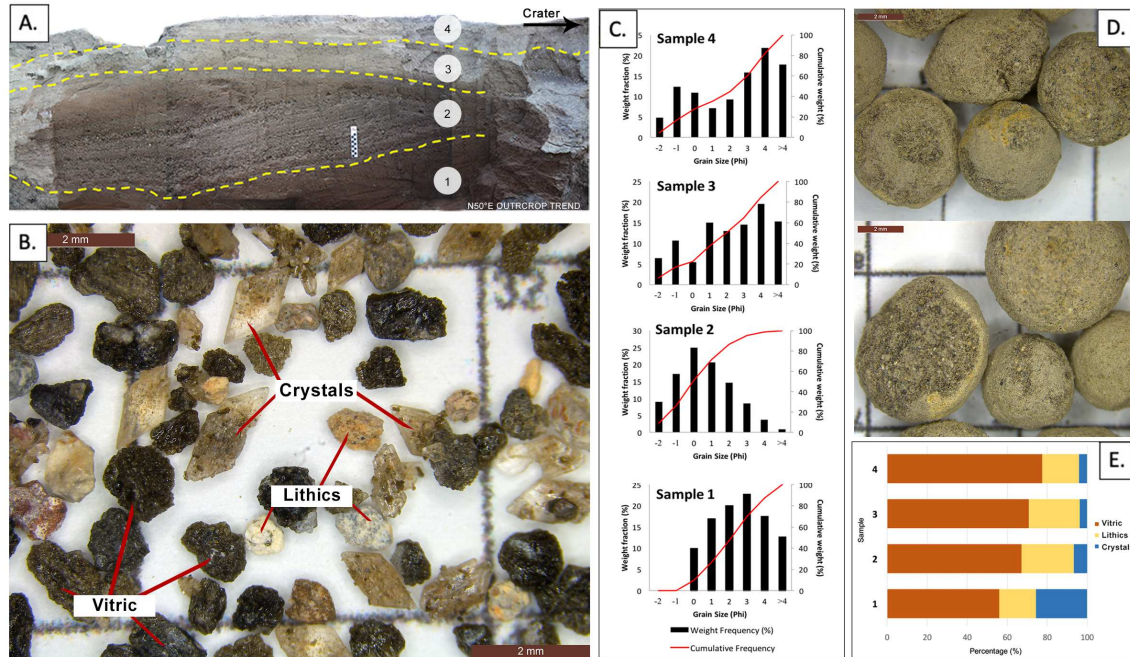


Figure 4: A) Location 1 (14.002304, 121.008571) where samples were collected; B) Ash components including vitric, lithic, and crystals; C) Grain size distribution graph per sampled layer; D) Accretionary lapilli found in Samples 3 and 4; E) Relative abundance of the components of ash per sample.

Nearly all sections of dunes have cross-bedded structures with dipping planar beds inclined by about 5° - 18° (Figure 5). Foresets and backsets in many sections of dunes are typically truncated by overlying strata and are interpreted as limbs of earlier-formed dunes that were eroded at their crests by succeeding flows. In the lower slopes, backsets are steeper than foresets whereas in the proximal to medial areas where the underlying slopes are steeper, the opposite is observed (see discussion on stoss and lee angles above). There is aggradation or regression in the upstream direction and migration of the crest of stacked dunes towards the crater typical of antidunes (Figures 5C,E and F). However, there were two adjacent outcrops beside a gully where migration of the crest of stacked dunes is toward the downstream direction (Figure 5D).

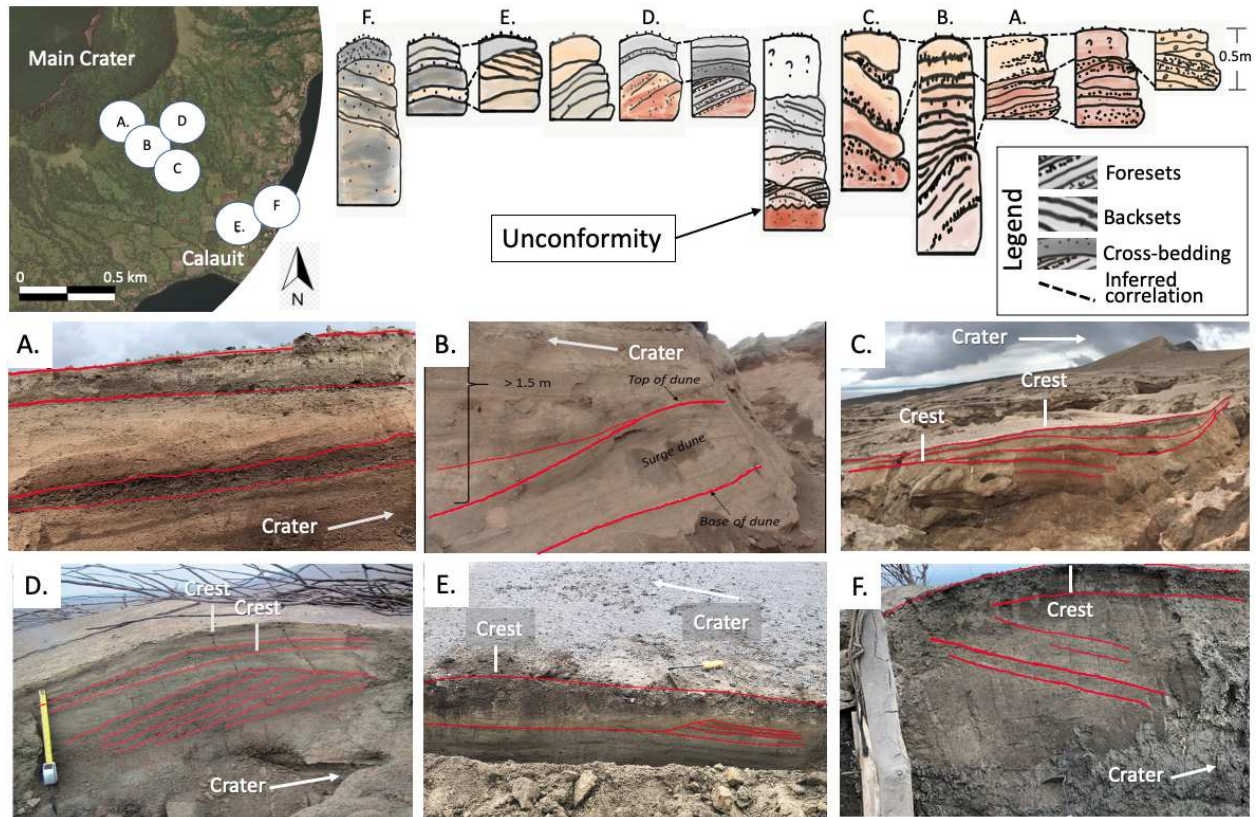


Figure 5: Stratigraphy of different dune bedforms in the southeast sector of TVI showing foresets, backsets, erosional features, curved surfaces, and ballistic fragments on the surface. See locations designated by letters A-F.

Volcanic glass (vitric), lithics, and crystal fragments comprise the base surge beds (Figure 4C). The vitric component is commonly light brown to black, translucent, and exhibits blocky, scoriaceous, and fluted forms. Bubble wall shards with varying vesicularity were observed in some fractions but with dominance of blocky vitric components suggestive of a phreatomagmatic eruption origin⁴⁰. Lithic fragments plucked from the wall rock or conduit, include sub-rounded rock fragments, oxidized grains, as well as hydrothermal fragments such as those observed in hydrothermal ore deposits (white to yellow with sulfides). Crystal components consist of euhedral to fragmented free crystals, with some still embedded in glassy groundmass. All samples contain the 3 tephra components, but are generally dominated by volcanic glass (56%-77%) with varying morphologies. Lithics are composed of 18%-26% hydrothermal fragments with an insignificant amount of rock grains. Crystal fragments have the lowest portion in all the layers (<25%).

Impacts Previously vegetated areas in the southeast sector of TVI was reduced to a desert dune field with fallen trees, ruptured bamboo, and splintered tree trunks (Figures 6A-B). The unidirectional blowdown was pronounced near large gullies where base surges were funneled. Trees were debarked and sandblasted mainly on the side facing the main explosion crater with some scorched but not completely turned into charcoal (Figures 6C). This suggests that these wet surges were at a minimum temperature of 200°C^{41,42}. In this part of the island, regrowth of trees a year after the 2020 eruption is not evident.

Velocity of the base surges near the crater rim is estimated to be ~50-60 ms⁻¹ based on video analysis. Downstream but within the upper slopes, velocities of 35.5-48.5 ms⁻¹ were calculated

based on PYFLOW v2.0⁴³ simulations using the grain size and componentry data (Figure 4A). Splintered *Ceiba pentrada*⁴⁴ in the lower mid-slopes (Figure 6A) indicate dynamic pressures in excess of 1.46-2.1 kPa^{42,45} and velocities of 31.3-37.5 ms⁻¹ using a density of 3.0 kgm⁻³, the same density computed by PYFLOW v2.0 which is within the range of values for dilute surges⁴⁶. Further downslope, a ruptured bamboo located beside a gully (Figure 6B) indicate dynamic pressures in the range of 0.9-1.71 kPa and velocities of 25.3-33.8 ms⁻¹. Using the run-up height of surge deposits on a school wall (Figure 6D) near the coast, velocities of 6.9-10.4 ms⁻¹ were calculated using two analytical models⁴⁷. The computed velocities show a decreasing trend from the crater to the coast. These velocities are consistent with estimates using the energy-line method⁴⁸ and show deceleration despite a concave upward slope profile⁴⁹.

Buildings along the coast had collapsed roofs and were buried by about 1-2 m of base surge deposits. Some areas were plastered by vertically-oriented and bedded muddy coating. Scattered ballistic projectiles, mainly composed of scoria bombs and minor altered lithic fragments, are found on the surface of the surge deposit field. They range from lapilli- to block-sized clasts (10 cm), decreasing in size towards the coast.

3 Discussion

Base surges are considered as a main hazard of Taal Volcano. Mobile and water vapor-rich, they can travel up to 30 ms⁻¹ and bury everything in their path¹⁴. This work provides primary data and empirical information, useful to advance our understanding of base surges and evaluating

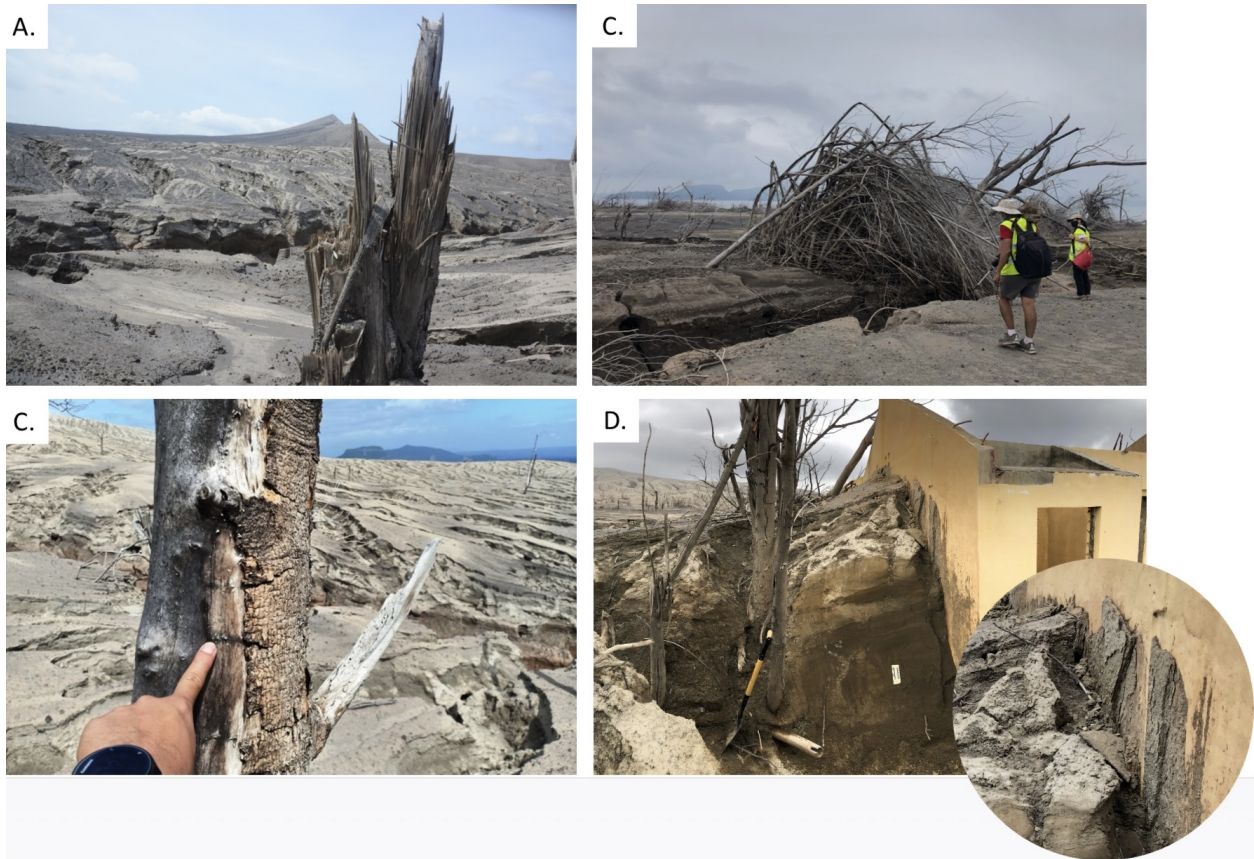


Figure 6: Photos of the effect of Base Surges on the southeast portion of TVI. A) Snapped and splintered tree trunk of *Ceiba pentrada* with trunk diameter ~ 0.5 m; B) Ruptured bamboo (Culm diameter = 12 cm); C) Scorched and debarked tree on the side facing the crater; D) Base Surge deposit run-up against school wall facing the crater. Inset photo shows plastered base surge deposits. This unique feature of pasty materials persistently sticking on walls is proposed to be called "ludite".

consequences and risks of such eruptions^{23,50}.

The 17-21 km-high 2020 phreatomagmatic eruption has equivalent mass discharge rates in the order of 10^7 kgm^{-3} with VEI=4. Base surges spread radially on the island from fountain collapse heights³¹ of ~ 360 m based on detailed analysis of photographs. A total base surge volume of ~ 16 million m^3 was deposited on the island beginning late afternoon, which most likely continued for another 10 hours based on peak activity as reviewed from official bulletins and seismic records. Topographic lows in the southeast and west of the MC rim allowed base surges to reach coastal areas extending ~ 600 m offshore the village of Calauit in the southeast sector of TVI.

A total of 480 families in Calauit were lucky to have evacuated the village hours before it was completely overwhelmed by lethal and destructive base surges. Unfortunately there was not enough lead time to evacuate 480 cattle, 270 horses, 70 carabaos, 276 goats, and more than a thousand swine and poultry⁵¹. All were declared in the livestock mortality report submitted to the Department of Agriculture.

Dunes characterize the base surge deposits on TVI. These elongated and sinuous mounds are perpendicular to sub-perpendicular to the direction of the density current as checked against the orientation of the blowdown of trees. Wave height to wavelength ratios of dunes partially plot in the moist PDC field of dunes studied worldwide. The unique morphometry of dunes in the mid-slopes and those nearer the coast, exhibiting smaller wave height to wavelength ratios, extend the field of moist PDCs. Dune profiles exhibit both progressive and regressive migration of dune crests, eroded foresets and backsets, cross stratification, pinch and swell draping, and

other sedimentary structures that provide a rich source of information that can contribute to the discussions on the flow regime and emplacement of pyroclastic density currents based on bedform characteristics^{10–12,37,42,52–55}.

Dynamic pressure and velocity estimates based on analysis of videos, numerical simulations, impact calculations for broken and splintered *Ceiba pentrada*⁴⁴ and ruptured bamboo, as well as run-up of surge deposits on a vertical school wall, show a decreasing trend from 50-60 ms⁻¹ from the crater to 35.5-48.5 ms⁻¹ in the upper middle slopes to 25.3-37.5 ms⁻¹ in the gullies of lower slopes to 6.8-10.4 ms⁻¹ near the shore. Structural impacts of these dynamic pressures on the village of Calautit were enough to destroy windows but not topple the walls of 1-storey buildings. The sequence of deposits suggest that the roof of houses collapsed due to tephra accumulation prior to the arrival of base surges. Lastly, computed velocities are consistent with estimates using the energy line model⁴⁸ and show that despite the concave upward slope profile of Taal Volcano, where acceleration is first to be expected before deceleration⁴⁹, the base surges decelerated from the crater rim to the coast (Figure 7).

4 Methodology

Review of images and videos Hundreds of photos taken by residents around Taal Lake, weekend tourists and passengers of commercial airplanes were reviewed to determine the type of eruption that took place on 12 January 2020 and 13 January 2020. Time-lapse videos taken by the authors on 13 January from Tagaytay, north of TVI, were also reviewed. Analysis of the photos include

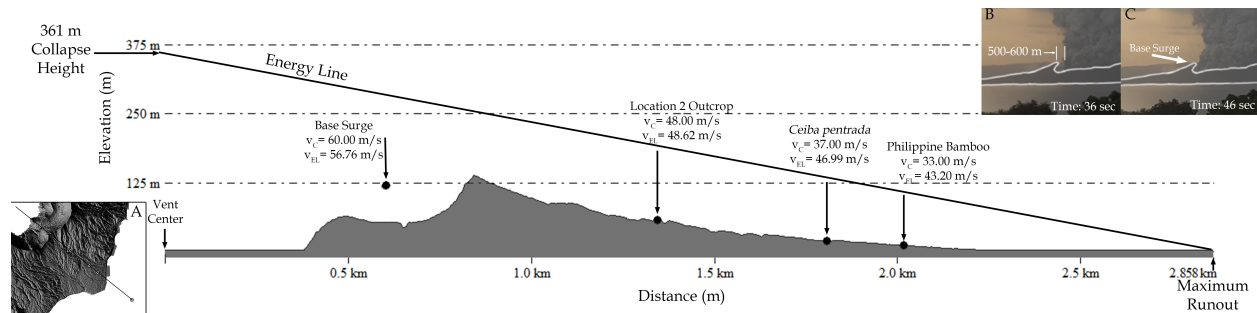


Figure 7: Projection of energy line model along the southeast profile of Taal Volcano Island where observation and calculation points for velocity are located from the vent center to the projected maximum runout distance. Velocities calculated using different methods (v_C) and velocities calculated using the energy line model (v_{EL}) for each of the four observation points are shown. A) Location of southeast profile and observation points. B) Image from timelapse video at 36 seconds showing 500-600 m open area within the southeast inner crater. C) Image from time-lapse video at 46 seconds showing the area from B being covered by a moving base surge.

the delineation of low areas of the MCL crater rim and possible overflow by PDCs above the rim. Available LiDAR DTMs for the whole island was used to delineate the pre-2020 topography of TVI and for the thickness analysis of newly-formed base surge deposits.

Field Work and Sample Collection Field surveys were conducted on January 30 and February 13, 2021, a little over a year after the eruption of Taal Volcano. Targeted areas in the 2-day fieldwork of the southeast portion of TVI were based on the analysis of photographs and remotely sensed imagery. Descriptions of the tephra stratigraphy were conducted along exposures in rills (≤ 1 meter deep) and gullies (3-7 meters deep) at the southeast flank of the volcano. Sections were scraped to expose the stratigraphy. Dunes were also scraped perpendicular to the elongation axis of mounds to expose internal structures.

Grain Size and Componentry Analysis At least 500g to 1kg of samples were collected per layer in the field to determine the size distribution of ash from individual layers. Grain size analysis

was conducted with manual sieving. Cone and quartered samples were dried overnight at 60°C to eliminate moisture. Sieving was performed using U.S.A. Standard Test Sieves ASTM E-11-20⁵⁶. Lithic, crystal, and vitric components were identified and described using a stereomicroscope, counting at least 1200 grains per sample.

DEMs from Drones An unmanned-aerial-vehicle (UAV) was used to obtain aerial imagery of parts of the southeastern sector of TVI. Selected regions of interest in the southeast sector were pre-programmed for mission flight paths covering areas of interest such as drainage, base surge dunes, and communities believed to have been overwhelmed by dilute PDCs. Sequential photos along the flight path were collected with 60% overlap to generate orthomosaic images, point-clouds, and DSMs.

Estimates of dynamic pressure and velocities A fountain collapse height (H) of 360 m was estimated³¹ based on the reconstruction of the vent location and the crater rim position in the southeast as derived from the review of photographs and videos (see supplementary video).

Dynamic pressures for the broken and splintered *Ceiba pentrada* and the ruptured bamboo were calculated using the following formula⁴⁵ (Equation 1)

$$P_{dyn} = \frac{1}{4} \frac{\pi r^2 \sigma_{ult}}{C_D h_o^2} \quad (1)$$

where P_{dyn} is the dynamic pressure, r is the radius of the tree, σ_{ult} is the yield strength of

Ceiba pentrada (29,600 kPa)⁴⁴ and Bamboo (150,000 kPa)⁵⁷, $C_D = 1.1$ and h_o are the estimated heights of the tree (25-30 m) and bamboo (15-25 m).

Probability density functions of flow properties (velocity and bulk density) and impact parameters (e.g. dynamic pressure) were calculated based on the grain size and componentry analysis at the sampled outcrop (14.002304, 121.008571) using PYFLOW v2.0⁴³. A mean flow density of 3.0 kgm^{-3} and dynamic pressures of 1.9-3.5 kPa were used in the velocity estimation using the following (Equation 2):

$$P_{dyn} = \frac{1}{2}\rho v^2 \quad (2)$$

where ρ is the density and v is the velocity. Rearranging Equation 2 yields to the following:

$$v = \sqrt{\frac{2P_{dyn}}{\rho}} \quad (3)$$

Equation 3 was subsequently used to compute for the flow velocities at the location of the *Ceiba pentrada*, the ruptured bamboo, and the sampled outcrop.

Using a minimum run-up height (H_r) of 2.5 m and a flow height (h_o) of 0.5 m at the location of a school near the coast, the following formulae for the momentum jump model (Equation 4) and the smooth momentum flux model (Equation 5) from Iverson et al., (2016)⁴⁷ (Appendix A7 and B13, respectively), were used to estimate the flow velocity at the school:

$$\frac{\rho_1}{\rho_0} \left(\frac{H_r}{h_0} \right)^3 - \left(\frac{H_r}{h_0} \right)^2 - \left(\frac{2}{\kappa} \text{Fr}_0^2 + 1 \right) \left(\frac{H_r}{h_0} \right) + \frac{\rho_0}{\rho_1} = 0 \quad (4)$$

$$H_r = \frac{\left(v + \frac{\kappa \rho_1 g h_0}{2 \rho_0 v} \cos^3 \theta \right)^2}{g \left(1 + \frac{\tan \phi}{\tan \theta} \right)} \quad (5)$$

Substituting the relationship $\text{Fr}_0 = v/\sqrt{gh_0}$ in Equation 4, the initial flow velocity using the momentum jump model was calculated. The momentum jump model considers a sudden jump in the momentum when the flow encounters an obstacle, forcing the initial flow velocity to decelerate to 0 m/s and causing an upward jump of the flow's surface elevation. On the other hand, the smooth momentum flux model considers a smooth transfer of mass and momentum from the flow's body to its head during run-up on an adverse slope with angle of inclination $\theta = 90^\circ$ (school wall) and basal friction angle $\phi = 8^\circ$ (slope gradient). These solutions assume equal densities of the incoming flow (ρ_o) and the flow on the adverse slope (ρ_1), and a pressure coefficient (κ) of 1.

Energy-line velocities The mobility ratio (H/L) was calculated based on the observed collapse height (H = 360 m) from the time-lapse video whereas the run-out distance (L = 2,858 m) was measured from the center of the vent to the farthest extent of the dunes observed towards the coast. The resulting mobility ratio was plotted on a log-normal relationship showing the PDC's volume and mobility with 95% confidence and prediction limits⁴⁸.

The maximum potential velocity of PDCs (Equation 6)⁴⁸ was derived based on the projected energy line model from the eruptive center of TVI.

$$v = (2g\Delta h)^{\frac{1}{2}} \quad (6)$$

where v is the velocity, g is the acceleration due to gravity and h is the vertical distance between energy line and the ground surface. Points where velocity was observed or calculated using other methods were then plotted along the energy line profile to compare the resulting potential velocities from the energy line model (Figure 7).

Limitations Only deposits in the southeastern areas of TVI are described in this paper with what can be accomplished in the span of two days of fieldwork with Alert Level 1 (Abnormal) hoisted over the entire Taal Volcano Island and Covid-19 modified quarantine restrictions still in place.

1. PTCC. Are you affected? (1991). URL <https://fb.watch/4mw1qqclqI/>.
2. Perttu, A. *et al.* Estimates of plume height from infrasound for regional volcano monitoring. *Journal of Volcanology and Geothermal Research* **402**, 106997 (2020).
3. Bachmeier, S. Eruption of the Taal Volcano in the Philippines CIMSS Satellite Blog (2020). URL <https://cimss.ssec.wisc.edu/satellite-blog/archives/35406>.
4. Cinco, M. Man found dead on Taal's Volcano Island (2020). URL <https://newsinfo.inquirer.net/1229252/man-found-dead-on-taals-volcano-island>.
5. PHIVOLCS. Taal Volcano profile, In: *Compilation of Eruptive History and Geology of Taal Volcano*. Tech. Rep., PHIVOLCS-Library (1991).

6. Saderra Maso, M. The eruption of Taal Volcano. *Bureau of Printing Manila Philippines* (1911).
7. Moore, J. G., Nakamura, K. & Alcaraz, A. The 1965 eruption of taal volcano. *Science* **151**, 955–960 (1966).
8. Delos Reyes, P. J. *et al.* A synthesis and review of historical eruptions at Taal Volcano, Southern Luzon, Philippines. *Earth-science reviews* **177**, 565–588 (2018).
9. Stoye, E. Tardigrade circus and a tree of life - January's best science images. *Nature* (2021). URL {<https://www.nature.com/immersive/d41586-021-00095-y/index.html>}.
10. Douillet, G. A. *et al.* Dune bedforms produced by dilute pyroclastic density currents from the august 2006 eruption of tungurahua volcano, ecuador. *Bulletin of Volcanology* **75**, 1–20 (2013).
11. Douillet, G. A. *et al.* Pyroclastic dune bedforms: macroscale structures and lateral variations. examples from the 2006 pyroclastic currents at tungurahua (ecuador). *Sedimentology* **66**, 1531–1559 (2019).
12. Smith, G. *et al.* A bedform phase diagram for dense granular currents. *Nature Communications* **11**, 1–11 (2020).
13. Moore, J. Base surge in recent volcanic eruptions. *Bulletin Volcanologique* **30**, 337 (1967).

14. Hickson, C. J. *Base Surge*, 41–42 (Springer Netherlands, Dordrecht, 2013). URL https://doi.org/10.1007/978-1-4020-4399-4_22.
15. PHIVOLCS. Summary of barangays susceptible to volcano base surge (2020). URL https://www.phivolcs.dost.gov.ph/vault/pdf/News/2020/BarangaysAtRisk_Taal_BaseSurge-Buffer.pdf.
16. Nemeth, K. & Kosik, S. Review of Explosive Hydrovolcanism. *Geosciences* **10**, 44 (2020). Number: 2 Publisher: Multidisciplinary Digital Publishing Institute.
17. Druitt, T. H. Pyroclastic Density Currents. *Geological Society, London, Special Publications* **145**, 145–182 (1998). Publisher: Geological Society of London.
18. Roche, O., Philips, J. & Karim, K. Pyroclastic Density Currents. In Fagents, S., Gregg, T. K. & Lopes, R. M. (eds.) *Modeling Volcanic Processes (The Physics and Mathematics of Volcanism)*, chap. 10, 203–229 (Cambridge University Press, Cambridge England, 2013).
19. Mastin, L. & Witter, J. The hazards of eruptions through lakes and seawater. *Journal of Volcanology and Geothermal Research* **2000**, 97 (195-214).
20. Belousov, A. & Belousova, M. Eruptive processes effects and deposits of the 1966 and the ancient basaltic phreatomagmatic eruptions in karymskoye lake, kamchatka, russia. *Special Publication International Association of Sedimentologists* **30**, 35–60 (2001).
21. Nemeth, K., Cronin, S., Charley, D., Harrison, M. & Garae, E. Exploding lakes in Vanuatu; “Surtseyan-style” eruptions witnessed on Ambae Island. *Episodes* **2006**, 87–92 (2007).

22. Dellino, P., Isaia, R., La Volpe, L. & Orsi, G. Interaction between particles transported by fall-out and surge in the deposits of the Agnano–Monte Spina eruption (Campi Flegrei, Southern Italy). *Journal of Volcanology and Geothermal Research* **133**, 193–210 (2004).
23. Brand, B. *et al.* A combined field and numerical approach to understanding dilute pyroclastic density current dynamics and hazard potential: Auckland volcanic field, new zealand. *Journal of Volcanology and Geothermal Reserach* **276**, 215–232 (2014).
24. Dufek, J., Esposti Ongaro, T. & Roche, O. Chapter 35 - pyroclastic density currents: Processes and models. In Sigurdsson, H. (ed.) *The Encyclopedia of Volcanoes (Second Edition)*, 617–629 (Academic Press, Amsterdam, 2015), second edition edn. URL <https://www.sciencedirect.com/science/article/pii/B9780123859389000353>.
25. Barberi, F. *et al.* Reducing volcanic disasters in the 1990's. *Bulletin Volcanological Society of Japan* **35 Series 2 No. 1**, 80–95 (1990).
26. Torres, R. & Punongbayan, R. Attention focuses on Taal: Decade volcano of the Philippines. *EOS* **76;24**, 241–247 (1995).
27. Cas, R. IAVCEI: From Small Beginnings to a Vibrant International Association. *Hist. Geo Space Sci.* **10**, 181–192 (2019).
28. Thomas, P. C. *et al.* Bright dunes on Mars. *Nature* **397**, 592–594 (1999).
29. Jackson, D. W., Bourke, M. C. & Smyth, T. A. The dune effect on sand-transporting winds on Mars. *Nature Communications* **6**, 1–5 (2015).

30. Smith, K. T. Ghost dunes spotted on mars. *Science* **361**, 376–377 (2018).
31. Sparks, R. *et al.* *Volcanic plumes* (John Wiley and Sons, Inc, United States, 1997).
32. Constantinescu, R. *et al.* The radius of the umbrella cloud helps characterize large explosive volcanic eruptions. *Communications Earth & Environment* **2**, 1–8 (2021).
33. PHIVOLCS. Taal Volcano eruption update 13 January 2020 04:00 PM (2020). URL <https://www.phivolcs.dost.gov.ph/index.php/taal-volcano-bulletin-menu/9633-eruption-update-for-taal-volcano-13-january-2020-04-00-pm>.
34. Moorhouse, B. L. & White, J. D. Interpreting ambiguous bedforms to distinguish subaerial base surge from subaqueous density current deposits. *The Depositional Record* **2**, 173–195 (2016).
35. Cole, P. Migration direction of sand-wave structures in pyroclastic-surge deposits: implications for depositional processes. *Geology* **19**, 1108–1111 (1991).
36. Crossweller, H. S. *et al.* Global database on large magnitude explosive volcanic eruptions (IAMEVE). *Journal of Applied Volcanology* **1**, 1–13 (2012).
37. Fisher, R. V. & Waters, A. C. Base surge bed forms in Maar volcanoes. *American Journal of Science* **268**, 157–180 (1970).
38. Schminke, H.-U., Fisher, R. V. & Waters, A. C. Antidune and chute and pool structures in the base surge deposits of the Laacher See area, Germany. *Sedimentology* **20**, 553–574 (1973).

39. Sigurdsson, H., Carey, S. & Fisher, R. The 1982 Eruptions of El Chichon Volcano, Mexico: The Physical Properties of Pyroclastic Surges. *Bulletin of Volcanology* **49**, 467–488 (1987).
40. Cas, R. & Wright, J. *Volcanic successions: modern and ancient* (London, Allen and Unwin, 1987).
41. Browne, F. Theories on the combustion of wood. Tech. Rep., Madison, Wis. : U.S. Dept. of Agriculture, Forest Service, Forest Products Laboratory (1958).
42. Brand, B. & Clarke, A. An unusually energetic basaltic phreatomagmatic eruption: using deposit characteristics to constrain dilute pyroclastic density current dynamics. *Journal of Volcanology and Geothermal Research* **243**, 81–90 (2012).
43. Dioguardi, F. & Mele, D. Pyflow 2.0: A computer program for calculating flow properties and impact parameters of past dilute pyroclastic density currents based on field data. *Bulletin of Volcanology* **80:28**, 1–16 (2018).
44. Green, D., Winandy, J. & Kretschmann, D. *Wood handbook - Wood as an Engineering material* (U.S. Department of Agriculture, Forest Service, Forest Products Laboratory, 1999).
45. Clarke, A. & Voight, B. Pyroclastic current dynamic pressure from aerodynamics of tree or pole blow-down. *Journal of Volcanology and Geothermal Research* **100**, 395–492 (2000).
46. Valentine, G. A. Stratified flow in pyroclastic surges. *Bulletin of Volcanology* **49**, 616–630 (1987).

47. Iverson, R., George, D. & Logan, M. Debris flow runup on vertical barriers and adverse slopes. *Journal of Geophysical Research* **121**;12, 2333–2357 (2016).
48. Toyos, G., Cole, P. D., Felpeto, A. & Marti, J. A GIS-based methodology for hazard mapping of small volume pyroclastic density currents. *Natural Hazards* **41**, 99–112 (2007).
49. Valentine, G., Doronzo, D., Dellino, P. & de Tullio, M. Effects of volcano profile on dilute pyroclastic density currents: Numerical simulation. *Geology* **39**, 947–950 (2011).
50. Cole, P. D., Neri, A. & Baxter, P. J. Hazards from pyroclastic density currents. In *The Encyclopedia of Volcanoes*, 943–956 (Elsevier, 2015).
51. Robles, R. & Robles, T. Initial Visit to Jowivil Crater View Subdivision Balete, Batangas. Tech. Rep., First Asia Institute of Technology and Humanities (2020).
52. Fisher, R. Bed forms in base-surge deposits: Lunar implications. *American Journal of Science* **26**, 1349–1352 (1969).
53. Waters, A. C. & Fisher, R. V. Base surges and their deposits: Capelinhos and taal volcanoes. *Journal of Geophysical Research* **76**, 5596–5614 (1971).
54. Crowe, B. M. & Fisher, R. V. Sedimentary structures in base-surge deposits with special reference to cross-bedding, Ubehebe Craters, Death Valley, California. *Geological Society of America Bulletin* **84**, 663–682 (1973).

55. Cole, P. & Scarpati, C. A Facies Interpretation of the Eruption and Emplacement Mechanisms of the Upper Part of the Neapolitan Yellow Tuff, Campi Flegrei, Southern Italy. *Bulletin of Volcanology* **55**, 311–326 (1993).
56. International ASTM. Standard Specification for Woven wire Test Sieve Cloth and Test Sieves. Tech. Rep., ASTM International, West Conshocken, PA (2014).
57. Bamboo Import. Mechanical Properties of Bamboo (2021). URL <https://www.bambooimport.com/en/blog/what-are-the-mechanical-properties-of-bamboo>.

5 Acknowledgements

The authors would like to thank the First Asia Institute of Technology and Humanities (FAITH) Colleges, FAITH Botanic Gardens Foundation (FBGF), and the local government units of Balete, Batangas for collaborating and facilitating access to the southeast sector of Taal Volcano Island.

Figures

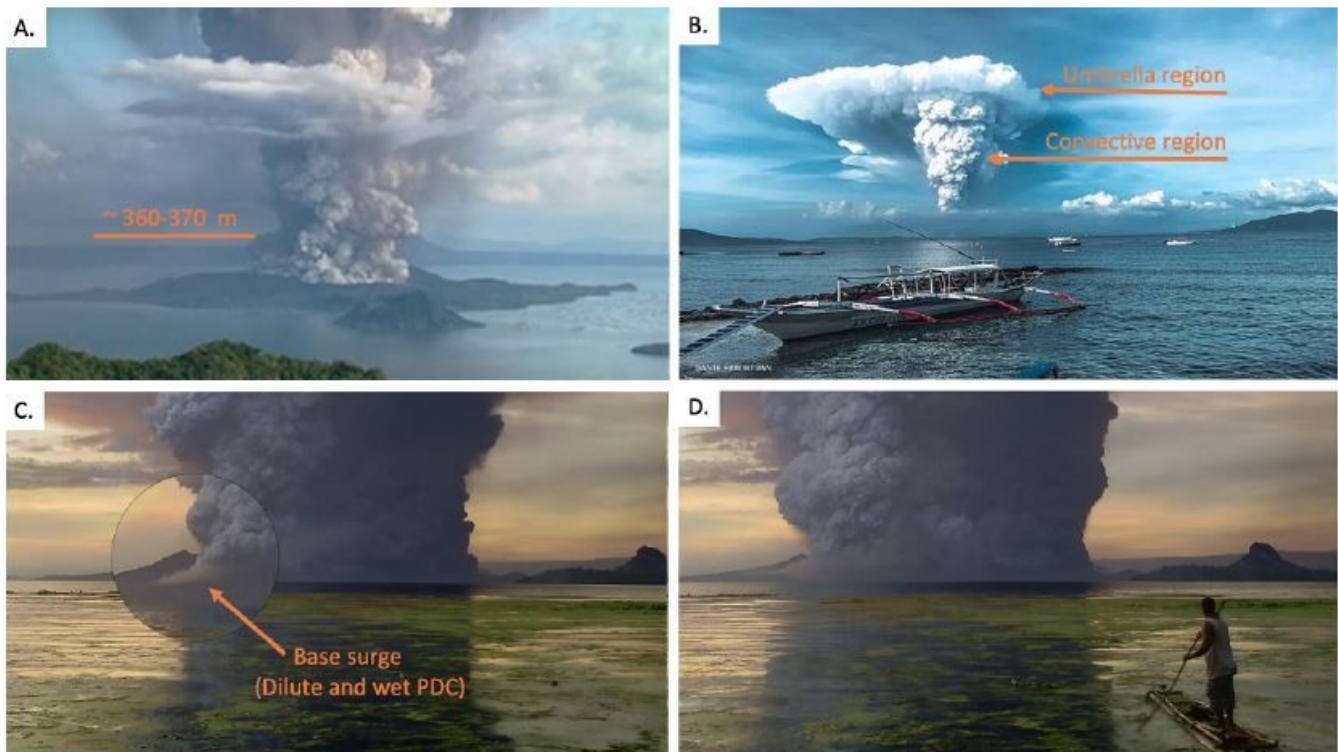


Figure 1

Photographs and screenshots of videos of the 12 January 2020 eruption of Taal. A) Eruption showing a lateral basal cloud with an estimated fountain height of 361 m; B) Umbrella cloud and convective regions; C) Magnified view of Base Surge flows (dilute and “wet” PDCs) forming in the southeast sector of TVI; D) Dust covering the southeastern slopes of TVI. Photo credits: Dante Pamintuan, CNN News and Andres Alisuag.

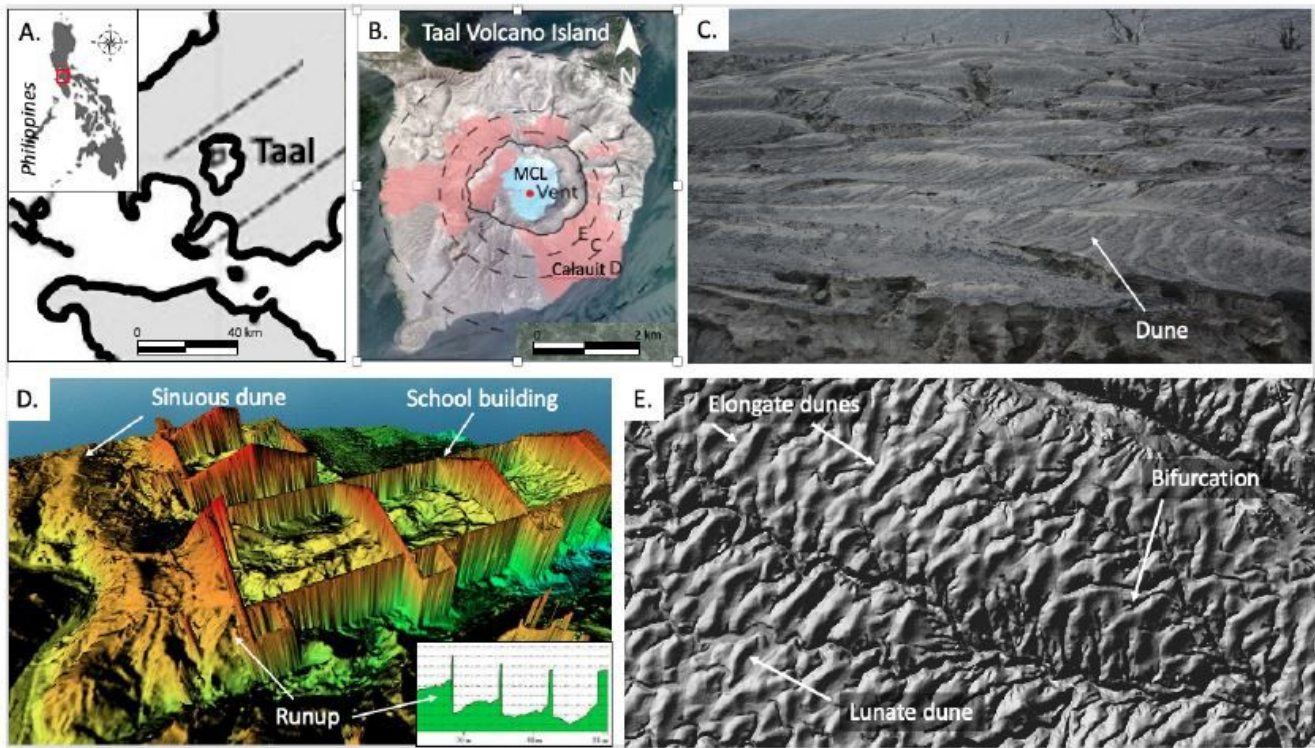


Figure 2

Dunes of TVI. A) General location of Taal Volcano Island. B) Distribution of the 2020 base surge dunes. Circles refer to upper slope, middle slope and lower slope boundaries. C) Photograph of the dune field. D) Digital Surface Model of school overwhelmed by base surges. Sinuous dunes and runup of the base surge also occur inside the classrooms. E) Plan view image of dunes showing elongate and lunate dunes. Bifurcation of dunes are also shown.

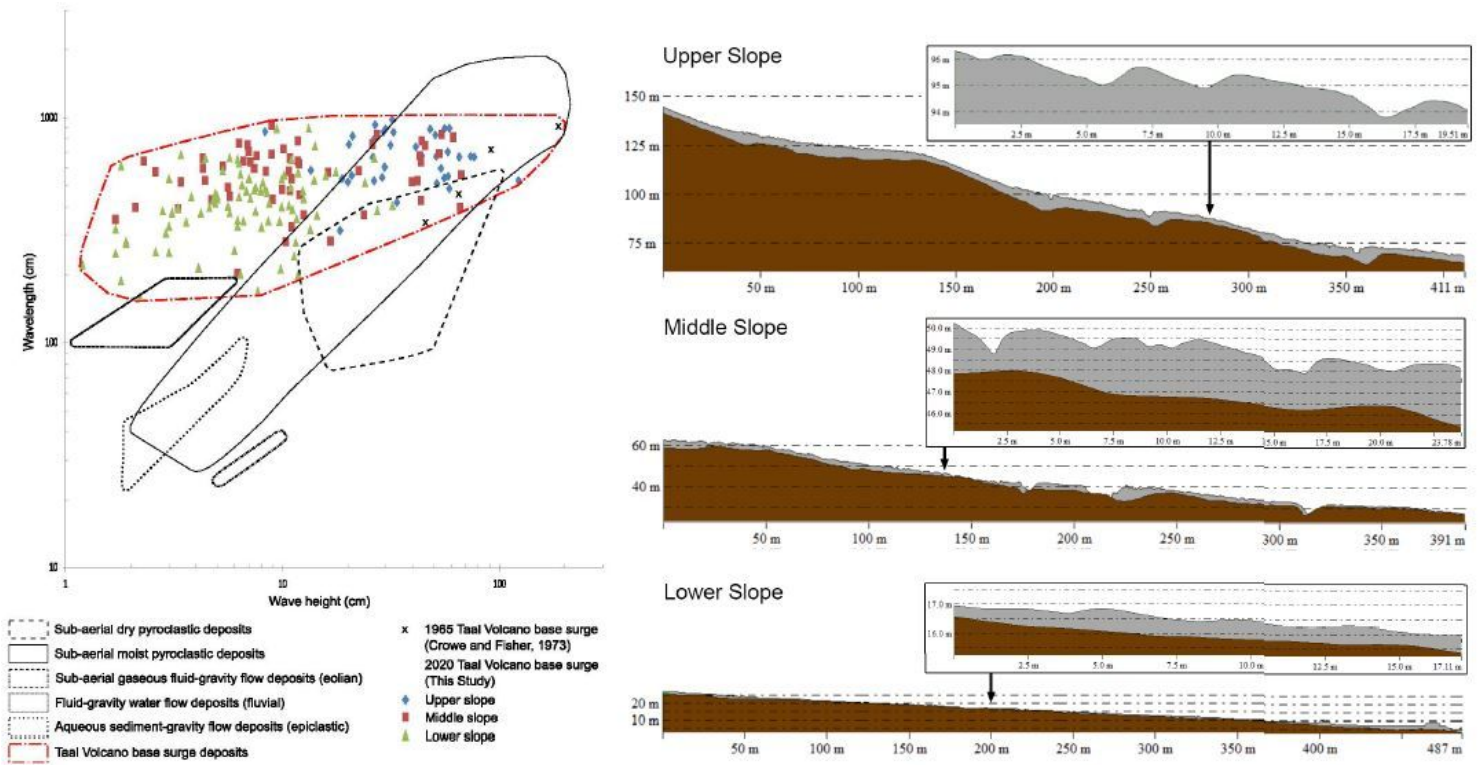


Figure 3

A) Graph of dune waveheight vs wavelength for subaerial dry and moist pyroclastic flows, eolian, fluvial and aqueous sediment-gravity (epiclastic) flows. Modified from Moorehouse and White (2016)34; B) Thickness of surge deposits in the upper, middle and lower slopes of the southeast sector of TVI. Profiles also show dunes with measured angles of stoss and lee sides at different gradients of underlying slope.

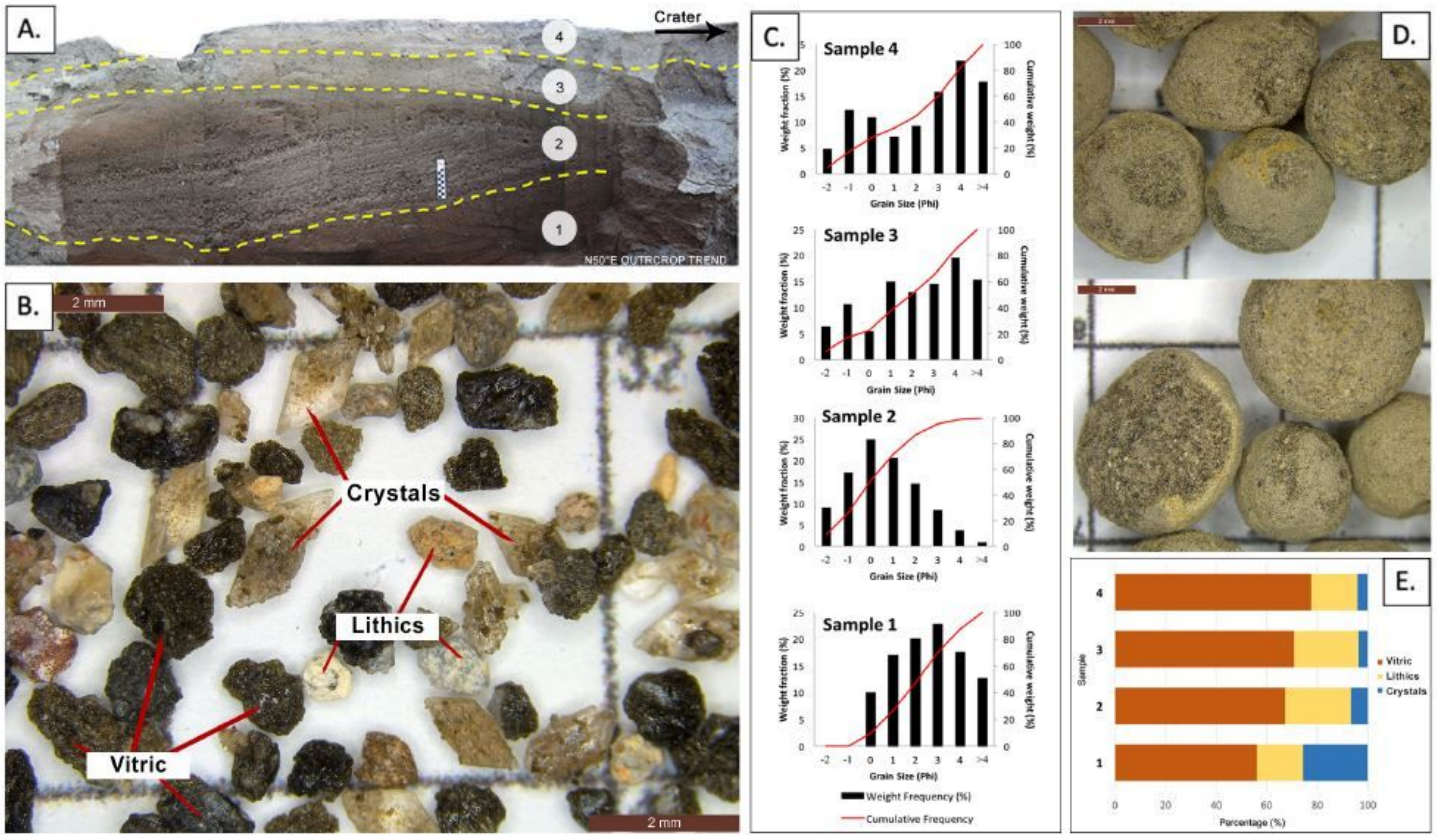


Figure 4

A) Location 1 (14.002304, 121.008571) where samples were collected; B) Ash components including vitric, lithic, and crystals; C) Grain size distribution graph per sampled layer; D) Accretionary lapilli found in Samples 3 and 4; E) Relative abundance of the components of ash per sample.

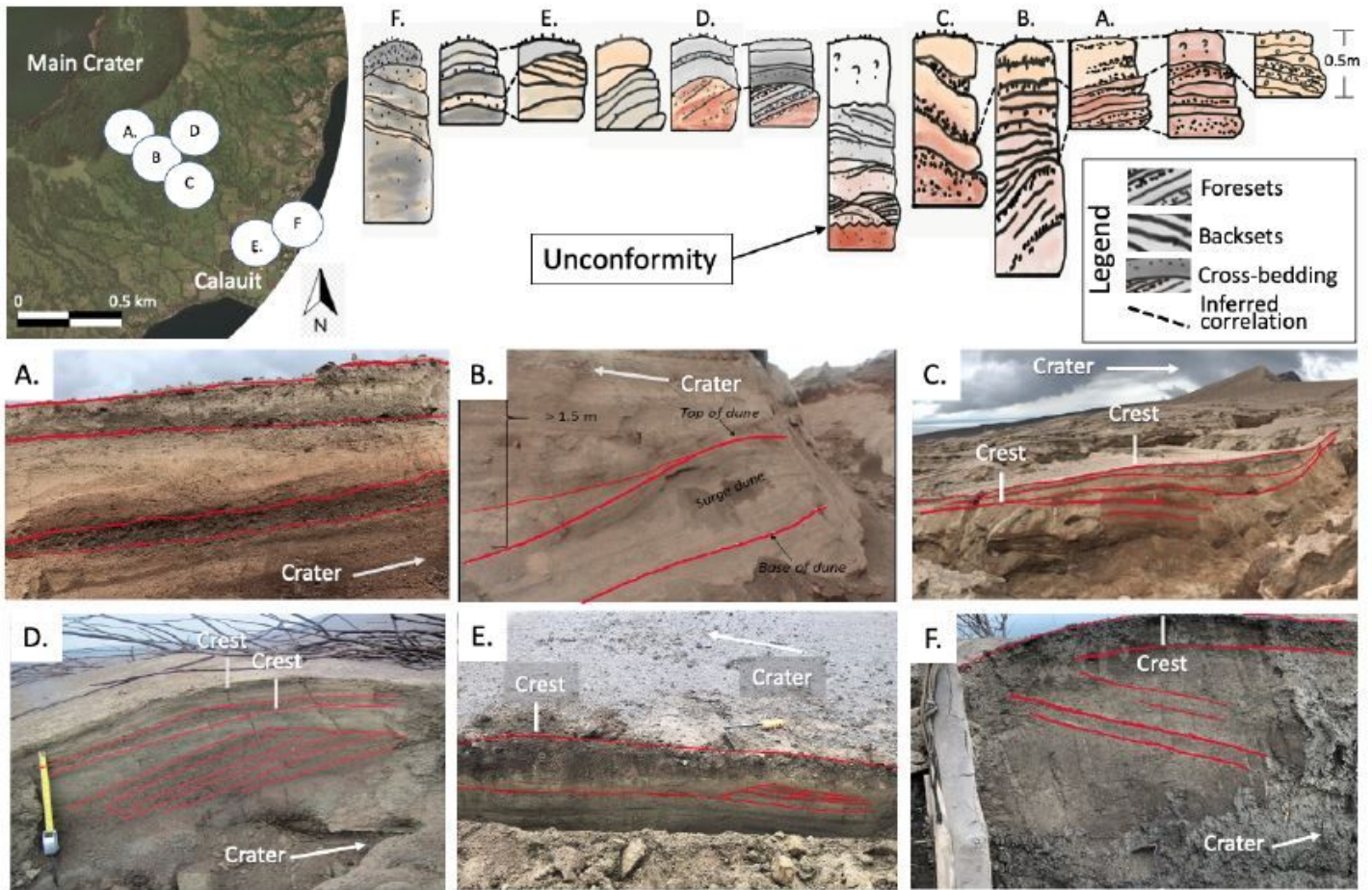


Figure 5

Stratigraphy of different dune bedforms in the southeast sector of TVI showing foresets, backsets, erosional features, curved surfaces, and ballistic fragments on the surface. See locations designated by letters A-F.

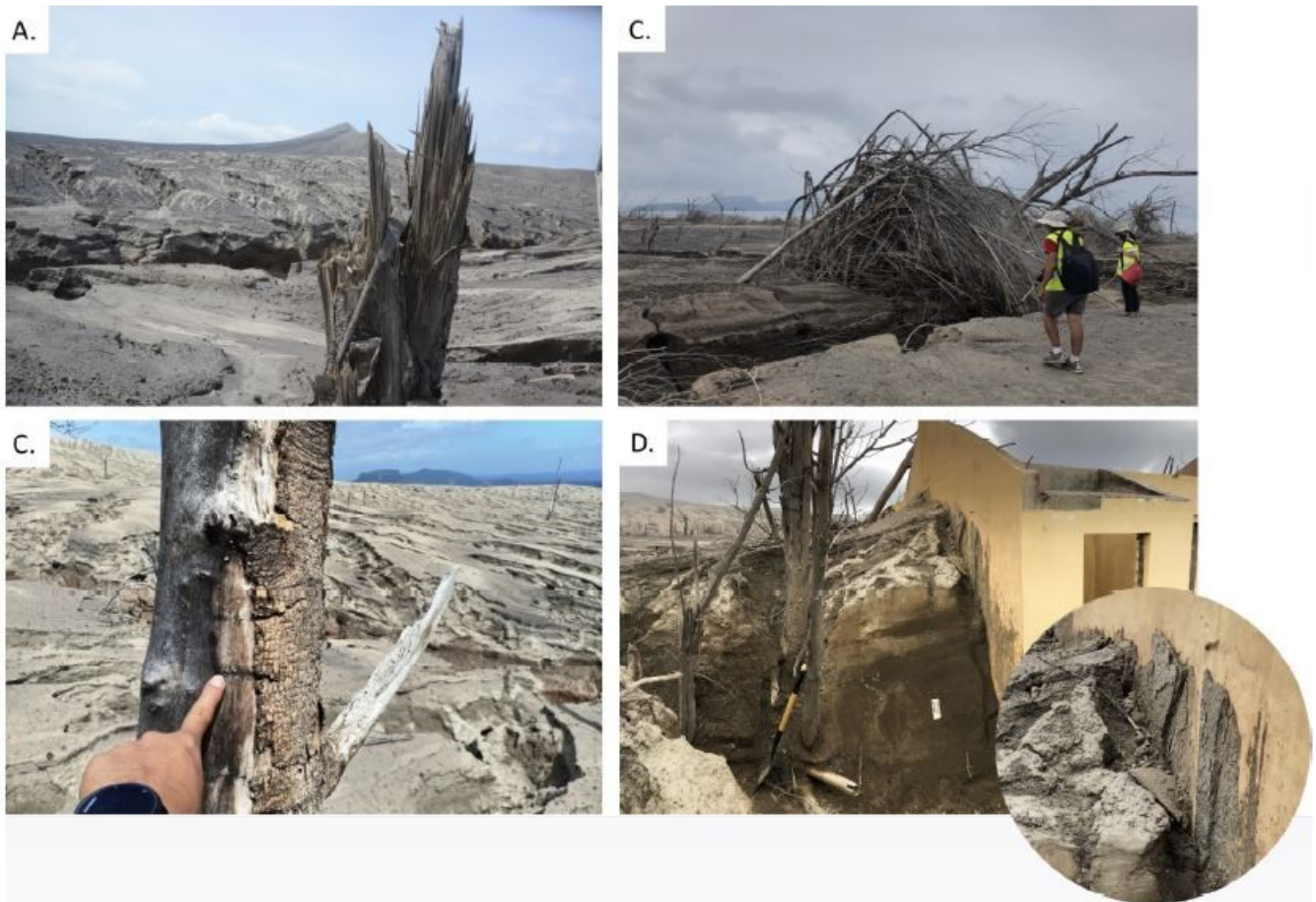


Figure 6

Photos of the effect of Base Surges on the southeast portion of TVI. A) Snapped and splintered tree trunk of *Ceiba pentrada* with trunk diameter ≈ 0.5 m; B) Ruptured bamboo (Culm diameter = 12 cm); C) Scorched and debarked tree on the side facing the crater; D) Base Surge deposit run-up against school wall facing the crater. Inset photo shows plastered base surge deposits. This unique feature of pasty materials persistently sticking on walls is proposed to be called "ludite".

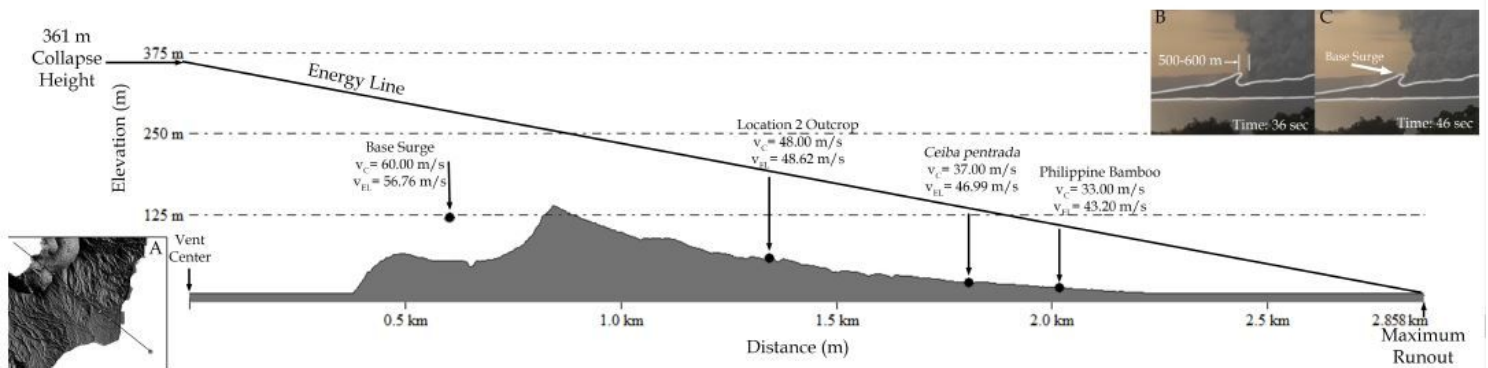


Figure 7

Projection of energy line model along the southeast profile of Taal Volcano Island where observation and calculation points for velocity are located from the vent center to the projected maximum runout distance. Velocities calculated using different methods (vC) and velocities calculated using the energy line model (vEL) for each of the four observation points are shown. A) Location of southeast profile and observation points. B) Image from timelapse video at 36 seconds showing 500-600 m open area within the southeast inner crater. C) Image from time-lapse video at 46 seconds showing the area from B being covered by a moving base surge.